Distributed Generator with Virtual Inertia Using Intelligent Controller for Grid-Connected Microgrid

Faa-Jeng Lin, *Fellow, IEEE*
Dept. of Electrical Engineering
National Central University
Chungli, Taiwan
linfj@ee.ncu.edu.tw

Kuang-Hsiung Tan
Dept. of Electrical and Electronic Engineering
Chung Cheng Institute of Technology, National Defense University
Taoyuan, Taiwan
s913115@gmail.com

Cheng-Ming Shih
Dept. of Electrical Engineering
National Central University
Chungli, Taiwan
stoneshih914@gmail.com

Abstract—**A grid-connected microgrid with virtual inertia using master/slave control is proposed to overcome the drawback of conventionally inverter-based distributed generators (DGs) for lacking of inertia. In this study, the microgrid consists of a storage system, a photovoltaic (PV) system and a three-phase resistive load. The storage system and PV system are considered as the master unit and the slave unit respectively in the microgrid. Moreover, since the grid codes demand the DGs to have the low-voltage ride through (LVRT) ability to help sustaining the stability of power system especially during the grid faults, the reactive power control should respond immediately during the grid faults according to the grid codes. Thus, for the purpose of improving the reactive power control in grid-connected microgrid and the transient response of microgrid during the switching between the grid-connected mode and islanding mode, an online trained recurrent wavelet fuzzy neural network (RWFNN) is proposed to replace the conventional proportional-integral (PI) controller in the storage system. Excellent control performance of the grid-connected microgrid with virtual inertia using the proposed intelligent RWFNN controller can be verified via some simulation results.**

Keywords—Microgrid, virtual inertia, low-voltage ride through, fuzzy neural network, wavelet function.

I. INTRODUCTION

Recently, owing to the growing awareness of environmental concerns and energy crisis, the penetration of distributed generations (DGs) using renewable energy source has been significantly increased in the power system [1]. Thus, a new opinion of microgrid to integrate the DGs and the loads at customer side has been arisen in the power system. The microgrid can be operated in either grid-connected mode or islanding mode. Moreover, the microgrid is considered as a small-scale power system and can improve grid performance and provide flexibility to its operation [2]. Thus, many different microgrids have been deployed in many countries and areas [3].

Conventional grid-connected power converters are normally operated as current sources and have no any frequency regulation capability. Therefore, the power system will be unstable resulted from the lack of rotating inertia if a large amount of inverter-based DGs is deployed [4], [5]. In other words, the dynamic responses of the inverter-based DGs are much faster than the conventional synchronous generator (SG) which will make the power system susceptible to oscillation resulting from sudden load variations or external disturbances [4], [6]. On the other hand, the SG possesses the ability of injecting the kinetic energy preserved in the rotating inertia to the power grid or absorbing the extra power energy

in the rotating inertia when sudden load variations or external disturbances occur. Owing to the merit of robustness of the rotating inertia, a lot of literatures for the inverter-based DGs using virtual synchronous generator (VSG) have been developed to emulate the virtual inertia by using the essential swing equation to mimic the transient characteristics of SG [7]-[9]. In [7], a full converter wind turbine with short-term minute-level energy storage adopted VSG control to represent the dynamic behavior of SG for supporting the power grid. Moreover, an improved VSG with bounded voltage and frequency has been proposed in [8] for smart grid integration. Furthermore, a new robust control adopted virtual inertia control to improve the frequency stability of an islanding microgrid was proposed in [9].

It is well known that a combination of neural networks (NNs) and fuzzy logic possesses the advantages of artificial learning in modeling the systems and the benefits of fuzzy reasoning in handling uncertain information. The combined fuzzy neural networks (FNNs) have been demonstrated being effective in different control applications [10]. Moreover, the wavelet transform has been widely used for analyzing the complicated time-varying signals due to its varied window function for the time domain [11]. Recently, the wavelet functions have been proposed to integrate into FNN to construct the wavelet fuzzy neural network (WFNN) for enhancing the adaptive and learning ability in complex engineering issues [12]. Furthermore, owing to the specific structure of a recurrent network with the internal feedback loop to capture system dynamics, the recurrent fuzzy neural network (RFNN) has better dynamic ability than the feed-forward form [13]. In addition, some researches have combined the recurrent structure with WFNN, i.e., the recurrent wavelet fuzzy neural network (RWFNN), and also has been successfully represented its applicability in various fields [14]. A new RWFNN with online training will be developed in this study.

Since the grid codes demand the DGs to have the LVRT ability to help sustaining the stability of power system especially during the grid faults. Thus, the reactive power control should be immediately responded during the grid faults according to the grid codes [15]. Moreover, the transient responses of three-phase voltages and currents in the microgrid during the switching between the grid-connected mode and islanding mode will cause serious influence on the customers' loads. Therefore, in this study, a microgrid with virtual inertia using master/slave control is developed to overcome the drawbacks of inverter-based DGs such as lack of the rotating inertia and without grid-forming capability. The developed microgrid comprises a storage system, a
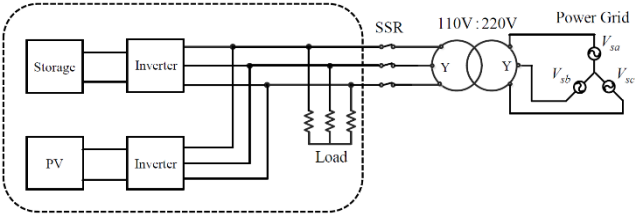
Fig. 1. Architecture of grid-connected microgrid.

photovoltaic (PV) system and a three-phase resistive load. Furthermore, the intelligent RWFNN controller is proposed to replace the traditional proportional-integral (PI) controller in the storage system to improve the reactive power control in grid-connected mode and the transient response of microgrid during the switching. In this study, the operating theories of the grid-connected microgird with virtual inertia will be detailedly presented in Section II. The network structure and online learning algorithms of the proposed RWFNN controller will be expressed in Section III. Then, the feasibility and effectiveness of the microgrid with virtual inertia using the proposed RWFNN controller to improve the reactive power control in grid-connected mode and the transient response of microgrid during the switching between the grid-connected mode and islanding mode will be verified by some simulation results in Section IV. Finally, some conclusions will be represented in in Section V.

II. GRID-CONNECTED MICROGRID WITH VIRTUAL INERTIA

The architecture of the grid-connected microgrid is illustrated in Fig. 1. The microgrid is composed of the storage system, PV system and a three-phase resistive load. The storage system and PV system are designed to be the master and the slave units respectively. The load is connected to the storage and PV systems in parallel to form the microgrid. The three-phase voltage of the microgrid is 110 Vrms. Moreover, the microgrid is connected to the three-phase power grid through a static switch relay (SSR) and a Y-Y connected transformer for transferring the voltage to a 220 Vrms distributed network.

A. Storage System with Virtual Inertia

The control blocks of DGs using master/slave control in microgrid is illustrated in Fig. 2. The storage system using active/reactive power control in grid-connected mode is provided in Fig. 2(a). In grid-connected operation, the voltage and frequency of the microgrid are imposed by the power grid. In Fig. 2(a), the three-phase voltages V_a, V_b, V_c of the microgrid and the three-phase current i_{oa}, i_{ob}, i_{oc} of the storage system are detected for the power calculation and synchronizing with power grid via the phase-lock-loop (PLL). The synchronous angle θ_e is obtained by the PLL. The three-phase voltages V_a, V_b, V_c and the three-phase currents i_{oa}, i_{ob}, i_{oc} are transferred to dq synchronous reference frame. Then, the active power output P_m and reactive power output Q_m of the storage system are calculated as follows:

$$P_m = \frac{3}{2}(V_q i_q + V_d i_d) \tag{1}$$

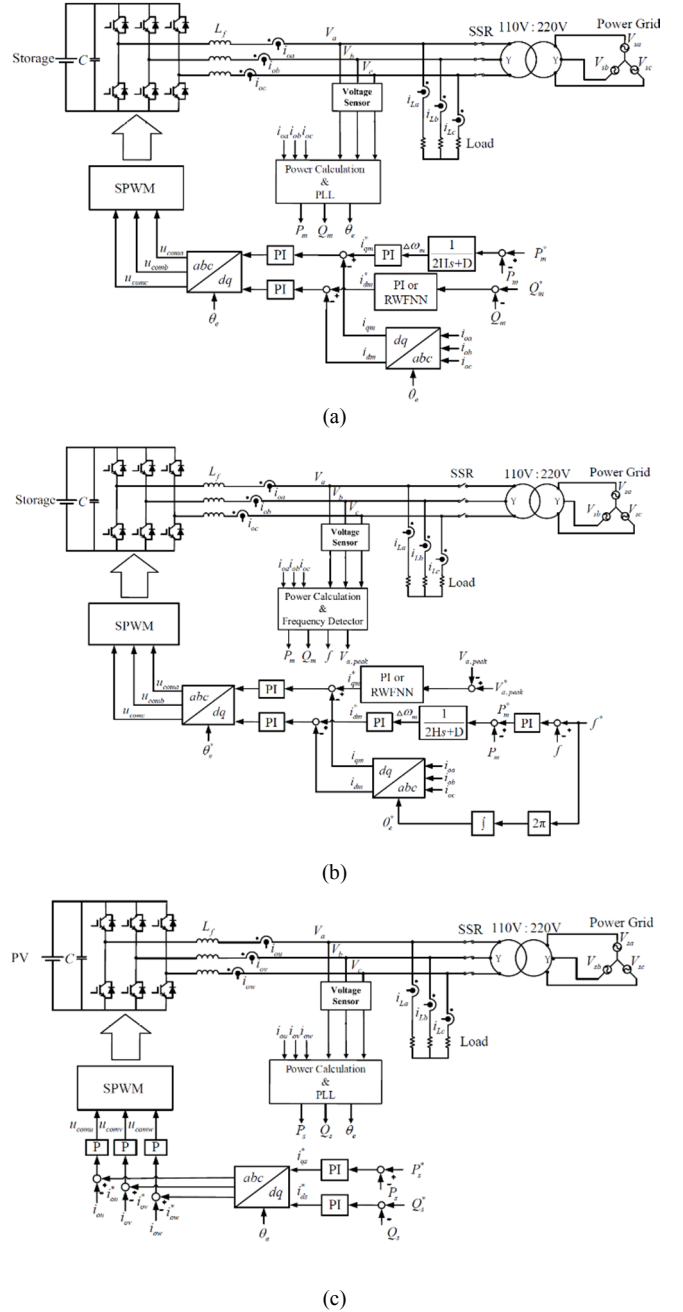$$Q_m = \frac{3}{2}(V_q i_d - V_d i_q) \tag{2}$$

(a)

(b)

(c)

Fig. 2. Control blocks of DGs using master/slave control in microgrid: (a) Storage system with virtual inertia in grid-connected mode. (b) Storage system with virtual inertia in islanding mode. (c) PV system in both grid-connected and islanding modes.

where V_d and V_q are the dq-axis voltages of the microgrid; i_d and i_q are the dq-axis currents of the storage system. In accordance with the PLL algorithm, the d-axis voltage V_d shown in (1) and (2) are set to be zero for the synchronization with the power grid. Therefore, the active power P_m and reactive power Q_m are proportional to i_q and i_d currents respectively as follows:

$$P_m = \frac{3}{2}V_q i_q \tag{3}$$

$$Q_m = \frac{3}{2}V_q i_d \tag{4}$$

In this study, to emulate the rotating inertia in the microgrid, the swing equation of SG is added in the storage system in the following [5], [16], [17]:

$$2H\frac{d\triangle\omega_m}{dt} = P_m^* - P_m - D\triangle\omega_m \qquad (5)$$

where H is the inertia constant; $\triangle\omega_m$ is the virtual angular velocity deviation in SG; D is the damping factor; P_m^* is the active power command of the storage system. According to the Laplace transform, the swing equation of SG can be rewritten as:

$$\triangle\omega_m = \frac{P_m^* - P_m}{2Hs + D} \qquad (6)$$

Then, the q-axis control current i_{qm}^* for the active power control is generated by a PI controller. Meanwhile, the d-axis control current i_{dm}^* for the reactive power control is obtained through a PI or the proposed RWFNN controller using the reactive power error as input. Finally, the control signals $u_{coma}, u_{comb}, u_{comc}$ are calculated through the dq/abc coordinate transformation to obtain the sinusoidal pulse width modulation (SPWM) switching signals for the storage system.

When the power grid is failed, the microgrid can immediately disconnect from the power grid via the SSR and smoothly switch the control mode from the active/reactive power control to the voltage/frequency control as shown in Fig. 2(b) to maintain the voltage and frequency of the microgrid. In Fig. 2(b), the peak value of the a-phase voltage $V_{a,peak}$ and the frequency f of the microgrid are gained by using the frequency detector. Then, the peak value of the a-phase voltage $V_{a,peak}$ and the frequency f of the microgrid are compared with the peak value of the phase voltage command $V_{a,peak}^*$ and the frequency command f^*. Thus, the q-axis control current i_{qm}^* for the voltage control is obtained through a PI or the proposed RWFNN controller. Meanwhile, the d-axis control current i_{dm}^* is obtained through the swing equation shown in (6) and a PI controller for maintaining the frequency of the microgrid. Finally, the control signals $u_{coma}, u_{comb}, u_{comc}$ are calculated through the dq/abc coordinate transformation with the angle command θ_e^* to obtain the SPWM switching signals for the storage system operated in islanding mode.

B. PV System

The PV system is considered as the slave unit and can provide active power and reactive power control in both the grid-connected mode and islanding mode. The control block of PV system is illustrated in Fig. 2(c). The three-phase voltages V_a, V_b, V_c of the microgrid and the three-phase currents i_{ou}, i_{ov}, i_{ow} of the PV system are detected and transferred to dq synchronous reference frame for the power calculation and synchronization. The errors of the active power and reactive power are both sent to the PI controllers for the generations of the dq-axis control currents i_{qs}^* and i_{ds}^* respectively. Moreover, the three phase current commands $i_{ou}^*, i_{ov}^*, i_{ow}^*$ are computed through the dq/abc coordinate
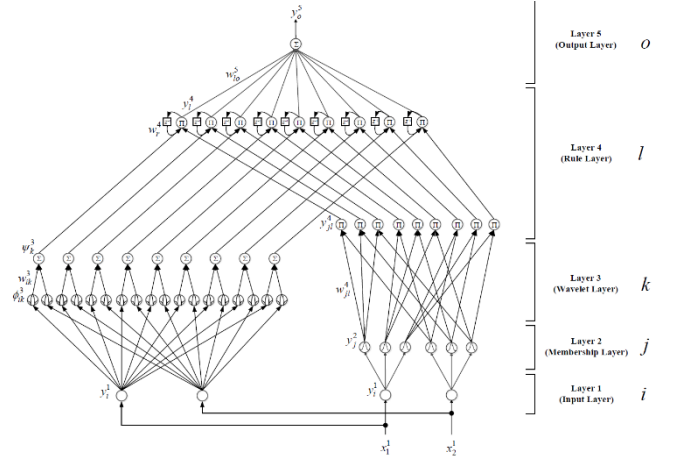

Fig. 3. Network structure of RWFNN.

transformation. Finally, the control signals $u_{comu}, u_{comv}, u_{comw}$ are calculated to obtain the SPWM switching signals for the PV system.

III. RWFNN

In this study, the intelligent RWFNN is proposed to replace the traditional PI controller in the storage system shown in Figs. 2(a) and (b) to improve the reactive power control in grid-connected mode and the transient responses during the mode switching. The network structure and the online learning based on backpropagation (BP) algorithm of the proposed RWFNN are expressed in detail as follows:

A. Network Structure

The network structure of the proposed RWFNN controller is represented in Fig. 3. Besides the input and output layer, there are three hidden layer in RWFNN including the membership layer, wavelet layer and rule layer. The signal propagation and the functions of each layer of RWFNN are depicted as follows:

1) Layer 1 (Input Layer): There are two input signals in this layer. One is the tracking error e of reactive power, and the other is its derivative $\dot{e}$. For every node i in this layer, its input and output are expressed as:

$$net_i^1(N) = x_i^1 \qquad (7)$$
$$y_i^1(N) = f_i^1(net_i^1(N)) = net_i^1(N), i = 1, 2; \qquad (8)$$

where x_i^1 is the input of ith node in this layer, and define x_1^1 as e while x_2^1 as $\dot{e}$; $net_i^1(N)$ expresses network inputs where superscript indicates the layer number and subscript indicates the node number; N is the number of the sampling iteration; $y_i^1(N)$ is the output of ith node; $f_i^1(\cdot)$ is a unity function.

2) Layer 2 (Membership Layer): In layer 2, the outputs of layer 1 are regarded as the inputs of this layer. Moreover, the membership function of this layer adopts the Gaussian function. The relationship between the input and output of each node is described below:

$$net_j^2(N) = -\frac{(x_i^2 - m_j^2)^2}{(\sigma_j^2)^2} \qquad (9)$$

$$y_j^2(N) = f_j^2(net_j^2(N)) = \exp(net_j^2(N)), j = 1, 2, ..., 6 \qquad (10)$$

where $x_i^2(N) = y_i^1(N)$ is the input; m_j^2 is the mean value of Gaussian function of jth node; σ_j^2 is the standard deviation

of Gaussian function of jth node; $y_j^2(N)$ is the output of jth node; $f_j^2(\cdot)$ is an exponential function.

3) Layer 3 (Wavelet Layer): The signal propagations of wavelet layer are depicted in the following:

$$\varphi_{ik}^3(x) = \frac{1}{\sqrt{|\sigma_{ik}^3|}}\left[1 - \frac{(x_i^1(N) - m_{ik}^3)^2}{(\sigma_{ik}^3)^2}\right]\exp\left[\frac{-(x_i^1(N) - m_{ik}^3)^2}{2(\sigma_{ik}^3)^2}\right] \quad (11)$$

$$,k = 1,2, ..., 9$$

$$\psi_k^3(N) = \sum w_{ik}^3 \varphi_{ik}^3(x) \quad (12)$$

where φ_{ik}^3 is the input of ith node from layer 1 to wavelet function of kth node; w_{ik}^3 is the connective weight; ψ_k^3 is the output of kth node in the wavelet layer; σ_{ik}^3 and m_{ik}^3 express the dilation variables and translation variables of the wavelet function, respectively.

4) Layer 4 (Rule Layer): This layer is composed of rule layer and recurrent layer. Each node l in this layer is denoted by Π, which multiplies the input signals and outputs the result of product. Moreover, the nodes of rule layer multiply the output signals from wavelet layer and recurrent layer, and output the result of product for dynamic mapping. They are summarized in the following:

$$y_{jl}^4(N) = \prod w_{jl}^4 y_j^2, \qquad l = 1,2,...,9 \quad (13)$$

$$net_l^4(N) = y_{jl}^4 \psi_k^3 w_r^4 y_l^4(N-1) \quad (14)$$

$$y_l^4(N) = f_l^4\left(net_l^4(N)\right) = net_l^4(N) \quad (15)$$

where $y_l^4(N)$ is the output of lth node in this layer; w_{jl}^4 is the connective weight between layer 2 and layer 4; w_r^4 is the recurrent weight; $y_l^4(N-1)$ stands for the previous output of lth node from this layer; $f_l^4(\cdot)$ is a unity function. The recurrent technique is adopted to incorporate a feedback loop in each node for dynamic mapping and higher sensitivity of previously obtained data.

5) Layer 5 (Output Layer): The outputs of layer 4 are regarded as the inputs of this layer. Moreover, the inputs are summed up as final output of this network. It can be obtained as follows:

$$net_o^5(N) = \sum_l^9 w_{lo}^5 x_l^5(N), \, o = 1 \quad (16)$$

$$y_o^5(N) = f_o^5(net_o^5(N)) = net_o^5(N) \quad (17)$$

where $x_l^5(N) = y_l^4(N)$ is the output from rule layer; w_{lo}^5 represents the connective weight; $y_o^5(N)$ depicts the final output of RWFNN, which means the current $i_{dm}^* = y_o^5(N)$ of storage system operated in grid-connected mode for the reactive power control and the current $i_{qm}^* = y_o^5(N)$ of storage system operated in islanding mode for the voltage control respectively; $f_o^5(\cdot)$ is a unity function.

B. Online Learning Algorithm

The detailed derivation of the online learning algorithms based on the back propagation learning rule. The objective of the back propagation algorithm is to minimize the energy function E, which is defined in the following:

$$E(N) = \frac{1}{2}(Q_m^* - Q_m)^2 = \frac{1}{2}e^2 \quad (18)$$

where Q_m^* and Q_m are defined as the reactive power command and the reactive power output of the storage system. The learning algorithm is represented in the following paragraphs.

1) Layer 5 (Output Layer): In layer 5, the gradient error of E in (18) with respect to the output of this layer is calculated as

$$\delta_o^5 = -\frac{\partial E}{\partial y_o^5(N)} = -\frac{\partial E}{\partial Q_m}\frac{\partial Q_m}{\partial y_o^5(N)} \quad (19)$$

$$\Delta w_{lo}^5 = -\eta_{lo}\frac{\partial E}{\partial w_{lo}^5} = -\eta_{lo}\frac{\partial E}{\partial y_o^5(N)}\frac{\partial y_o^5(N)}{\partial w_{lo}^5} = \eta_{lo}\delta_o^5 x_l^5 \quad (20)$$

where the factor η_{lo} is the learning rate. The connective weight w_{lo}^5 is updated in the following:

$$w_{lo}^5(N+1) = w_{lo}^5(N) + \Delta w_{lo}^5 \quad (21)$$

2) Layer 4 (Rule Layer): In layer 4, error terms need to be computed and propagated:

$$\delta_l^4 = -\frac{\partial E}{\partial y_l^4(N)} = -\left[\frac{\partial E}{\partial y_o^5(N)}\right]\frac{\partial y_o^5(N)}{\partial y_l^4} = \delta_o^5 w_{lo}^5 \quad (22)$$

$$\delta_{jl}^4 = -\frac{\partial E}{\partial y_{jl}^4(N)} = -\left[\frac{\partial E}{\partial y_o^5(N)}\frac{\partial y_o^5(N)}{\partial y_l^4(N)}\right]\frac{\partial y_l^4(N)}{\partial y_{jl}^4(N)} \quad (23)$$

$$= \delta_l^4 \varphi_k^3 w_r^4 y_l^4(N-1)$$

$$\Delta w_r^4 = -\eta_r\frac{\partial E}{\partial w_r^4} = -\eta_r\left[\frac{\partial E}{\partial y_o^5(N)}\frac{\partial y_o^5(N)}{\partial y_l^4(N)}\right]\frac{\partial y_l^4(N)}{\partial w_r^4(N)} \quad (24)$$

$$= \eta_r\delta_l^4 \psi_k^3 y_{jl}^4 y_l^4(N-1)$$

where the factor η_r is the learning rate. The recurrent weight w_r^4 is updated in the following:

$$w_r^4(N+1) = w_r^4(N) + \Delta w_r^4 \quad (25)$$

3) Layer 2 (Membership Layer): In layer 2, error term need to be propagated and computed:

$$\delta_j^2 = -\frac{\partial E}{\partial net_j^2} = -\left[\frac{\partial E}{\partial y_{jl}^4(N)}\right]\frac{\partial y_{jl}^4(N)}{\partial y_j^2(N)}\frac{\partial y_j^2(N)}{\partial net_j^2(N)} = \sum_{jl}\delta_{jl}^4 y_{jl}^4 \quad (26)$$

By means of the chain rule, the mean value and standard deviation of the Gaussian function can be computed by the following equations:

$$\Delta m_j^2 = -\eta_m\frac{\partial E}{\partial m_j^2} = -\eta_m\left[\frac{\partial E}{\partial net_j^2(N)}\right]\frac{\partial net_j^2(N)}{\partial m_j^2(N)} = \eta_m\delta_j^2\frac{2(x_i^2 - m_j^2)}{(\sigma_j^2)^2} \quad (27)$$

$$\Delta \sigma_j^2 = -\eta_\sigma\frac{\partial E}{\partial \sigma_j^2} = -\eta_\sigma\left[\frac{\partial E}{\partial net_j^2(N)}\right]\frac{\partial net_j^2(N)}{\partial \sigma_j^2(N)} = \eta_\sigma\delta_j^2\frac{2(x_i^2 - m_j^2)^2}{(\sigma_j^2)^3} \quad (28)$$

where the factors η_m and η_σ are the learning rates. The m_j^2 and σ_j^2 are updated according to the following equations:

$$m_j^2(N+1) = m_j^2(N) + \Delta m_j^2 \quad (29)$$

$$\sigma_j^2(N+1) = \sigma_j^2(N) + \Delta \sigma_j^2 \quad (30)$$

Due to the uncertainties of the system, the exact calculation of the sensitivity of the system $\partial Q_m / \partial y_o^5(N)$ cannot be determined exactly. Therefore, for the purpose of

solving this problem, the delta adaptation law is adopted to increase the online learning speed of the network parameters

$$\delta_o^5 \cong e + \dot{e} \qquad (31)$$

IV. SIMULATION RESULTS

In this study, to verify the feasibility and the effectiveness of the grid-connected microgrid with virtual inertia using the proposed RWFNN controller, the microgrid is realized via the PSIM simulation software. Moreover, two test conditions are designed in the simulation using PSIM: (1) the grid-connected mode, and (2) switching between grid-connected mode and islanding mode. Furthermore, to compare the performance of the microgrid using the proposed RWFNN controller, the simulation results using PI controlled storage system of the microgrid are also provided for the demonstration.

A. Grid-Connected Mode

In this mode, the grid-connected microgrid is equipped with 1 kW load. The active power command P_m^* of the storage system is changed from 0.5 kW to 1.5 kW and finally changed to 1 kW. The reactive power command Q_m^* of the storage system is changed from 0 Var to 0.5 kVar. Moreover, the active power command P_s^* and the reactive power command Q_s^* of the PV system are maintained to be 1.5 kW and 0 Var. First, in order to verify the effectiveness of the microgrid with virtual inertia using the master/slave control, the simulation result of the storage system using PI controllers without the virtual inertia is provided. The responses of the active power P_m and reactive power Q_m of the storage system using PI controllers without the virtual inertia are represented in Fig. 4(a). Moreover, the simulation results of the microgrid using PI controllers with the virtual inertia are provided in Figs. 4(b)-4(d). The responses of the active power P_m and reactive power Q_m of the storage system using PI controllers with the virtual inertia are represented in Fig. 4(b). The responses of the active power P_s and reactive power Q_s of the PV system are shown in Fig. 4(c). The responses of the active power P_{grid} and reactive power Q_{grid} of the power grid are illustrated in Fig. 4(d). According to the simulation result shown in Fig. 4(a), the transient response of the active power P_m of the storage system using PI controller tracks the power command promptly due to the absence of the virtual inertia. On the other hand, the transient response of the active power P_m of the storage system using PI controllers with the virtual inertia tracks the power command smoothly as shown in Fig. 4(b). Hence, the effectiveness and the feasibility of the microgrid with virtual inertia are verified. Furthermore, in accordance with the simulation results shown in Figs. 4(b)-4(d), since the microgrid is equipped with 1 kW load, the extra active power and reactive power of the storage system and PV system are dispatched to the distributed power grid as shown in Fig. 4(d). In addition, to improve the tracking control of the reactive power of the storage system, the RWFNN controller is proposed to replace the traditional PI controller in d-axis control current of the storage system shown in Fig. 2(a). Meanwhile, the q-axis control current of the storage system still adopts the PI controller with virtual inertia for the active power control. The simulation results of the microgrid using the proposed RWFNN controller with the virtual inertia are

shown in Figs. 4(e)-4(g). The responses of the active power P_m using PI controller and the reactive power Q_m using the proposed RWFNN controller of the storage system with the virtual inertia are represented in Fig. 4(e). The responses of the active power P_s and reactive power Q_s of the PV system are illustrated in Fig. 4(f). The responses of the active power P_{grid} and reactive power Q_{grid} of the power grid are expressed in Fig. 4(g). According to the simulation results shown in Figs. 4(b) and 4(e), the transient and steady-state responses of reactive power control of the RWFNN controlled storage system are better than the PI controlled storage system due to the merits of the proposed RWFNN controller such as the superior modeling performance and the capability to approximate the nonlinear systems and uncertainties. Additionally, the energy balance in power flow of the microgrid which the storage system uses the proposed RWFNN controller is also verified as shown in Figs. 4(e)-4(g). Therefore, the effectiveness of the microgrid with virtual inertia using the active and reactive power control are validated. Consequently, fast response of the reactive power control of the storage system using the proposed RWFNN controller is also certified.

B. Switching between Grid-Connected Mode and Islanding Mode

In this test case, the operation of the microgrid with 2 kW load is changed from the grid-connected mode in the interval 0-10 s to islanding mode in the interval 10-20 s due to the power grid fail at 10 s. The storage system and the PV system both adopts the active/reactive power control in grid-connected mode. Meanwhile, the voltage and frequency of the microgrid are imposed by the power grid. When the power grid interrupts, the storage system switches from the active/reactive power control to the voltage/frequency control to maintain the voltage and frequency of the microgrid. Moreover, the PV system still adopts the active/reactive power control in islanding mode. The active power command P_m^* and the reactive power command Q_m^* of the storage system are set to be 0.5 kW and 0 Var in grid-connected mode and the peak of the phase voltage command $V_{a,peak}^*$ and the frequency command f^* of the storage system are set to be 89 V and 60 Hz in islanding mode. The active power command P_s^* and the reactive power command Q_s^* of the PV system are maintained to be 0.5 kW and 0 Var in both the grid-connected mode and the islanding mode. First, the simulation results of the micrgorid using the PI controller during the switching between the grid-connected mode and the islanding mode are represented in Figs. 5(a)-5(d). The responses of the peak of the a-phase voltage and the frequency of the microgrid using the conventional PI controller are shown in Fig. 5(a). The responses of active power and reactive power of the storage and the PV systems are represented in Figs. 5(b) and 5(c). The responses of active power and reactive power of the power grid are illustrated in Fig. 5(d). According to the simulation result shown in Fig. 5(a), though the steady-state response of the voltage of the microgrid can be maintained corresponding to the voltage command of the storage system in islanding mode, the transient response of the voltage of the microgrid fluctuates seriously during the mode switching due to the poor robustness of the PI controller. Furthermore, in the interval 0-10 s, since the microgrid with 2 kW load is
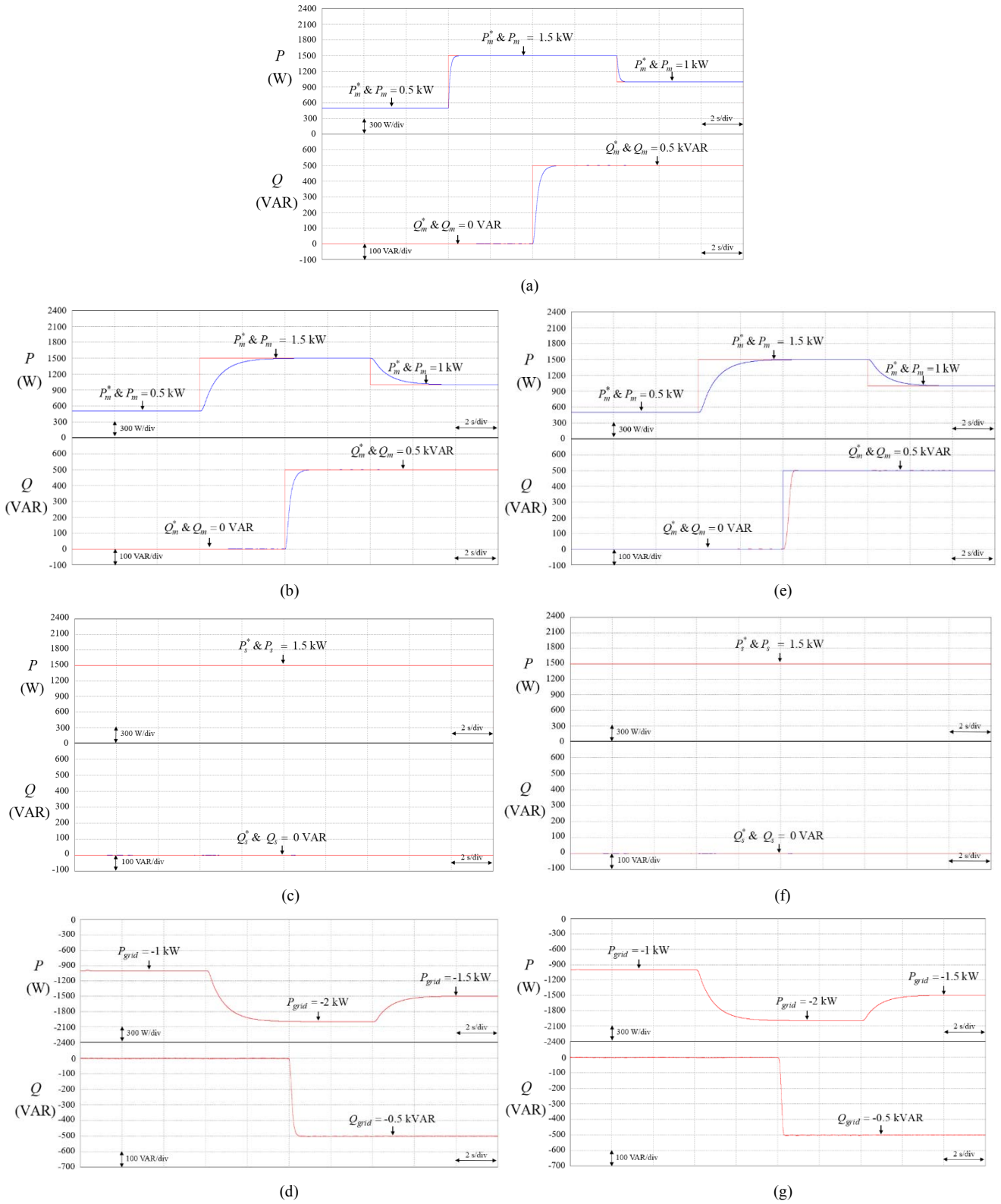
Fig. 4. Simulation results of grid-connected microgrid: (a) Responses of active power and reactive power of storage system using PI controller without virtual inertia. (b) Responses of active power and reactive power of storage system using PI controller with virtual inertia. (c) Responses of active power and reactive power of PV system. (d) Responses of active power and reactive power of power grid. (e) Responses of active power and reactive power of storage system using proposed RWFNN controller with virtual inertia. (f) Responses of active power and reactive power of PV system. (g) Responses of active power and reactive power of power grid.

connected with the power grid, the power grid delivers the active power 1 kW to the 2 kW load for the power demand shown in Figs. 5(b)-5(d). When the microgrid operates in islanding mode in the interval 10-20 s, the delivered power from the power grid reduces to be zero. In addition, since the storage system adopts the voltage/frequency control in the islanding mode to maintain the voltage and frequency, the storage system dispatches active power 1.5 kW to the load according to the load demand. Hence, the power balance of supply and demand can be guaranteed.
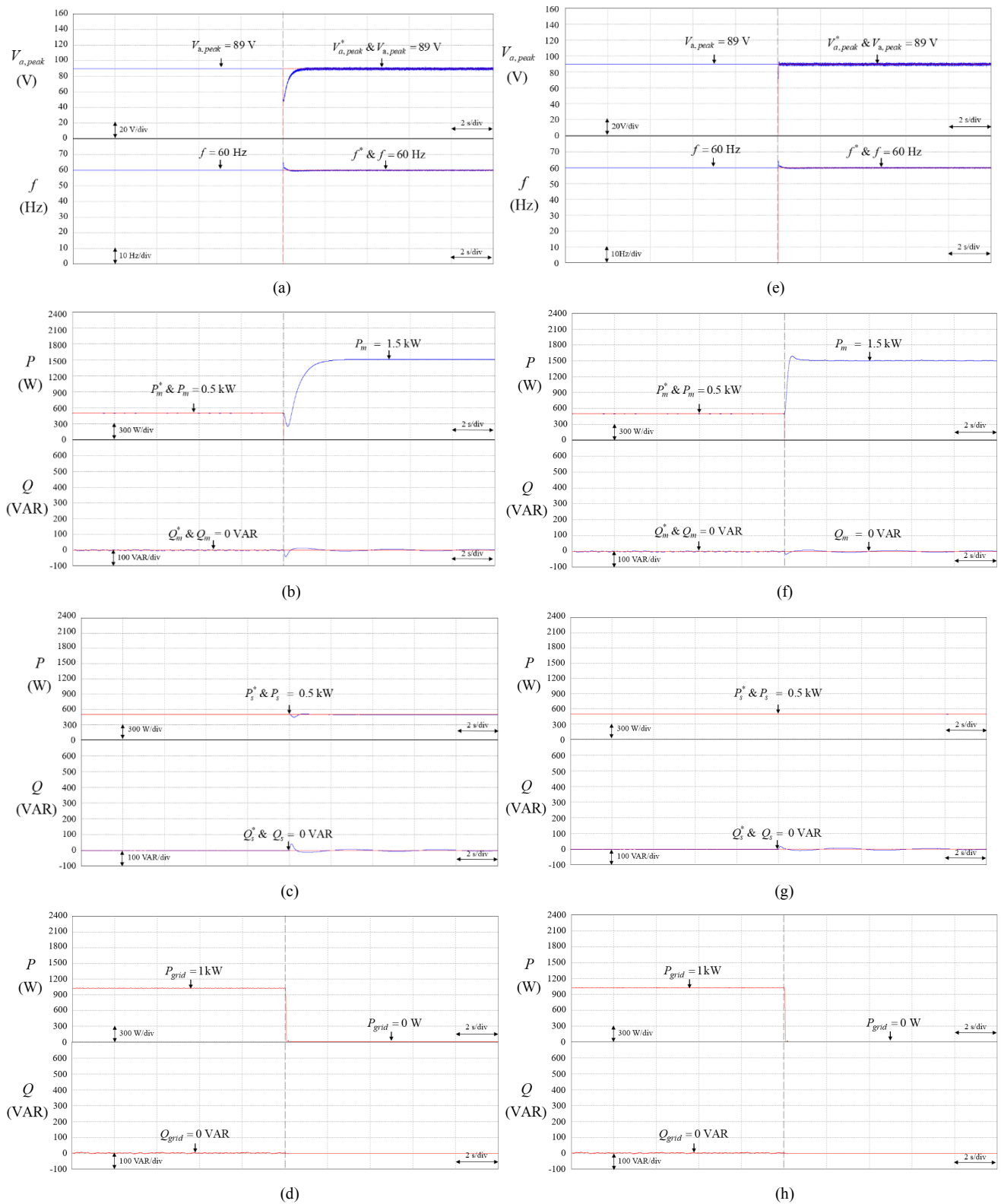
Fig. 5. Simulation results of microgrid during mode switching at 10 s: (a) Responses of peak of *a*-phase voltage and frequency of microgrid using PI controller. (b) Responses of active power and reactive power of storage system. (c) Responses of active power and reactive power of PV system. (d) Responses of active power and reactive power of power grid. (e) Responses of peak of *a*-phase voltage and frequency of microgrid using proposed RWFNN controller. (f) Responses of active power and reactive power of storage system. (g) Responses of active power and reactive power of PV system. (h) Responses of active power and reactive power of power grid.

To improve the transient response of the microgrid during the mode switching, the intelligent RWFNN controller is also proposed to replace the traditional PI controller in *q*-axis control current of the storage system operated in islanding mode for the voltage control as shown in Fig. 2(b). The

simulation results of the micrgorid using the proposed RWFNN controller during the switching between the grid-connected mode and the islanding mode are represented in Figs. 5(e)-5(h). The responses of the peak of the *a*-phase voltage and the frequency of the microgrid using the proposed

RWFNN controller are shown in Fig. 5(e). The responses of active power and reactive power of the storage and the PV systems are presented in Figs. 5(f) and 5(g). The responses of active power and reactive power of the power grid are provided in Fig. 5(h). Comparing to the simulation results shown in Figs. 5(a) and 5(b), the transient responses of the voltage of the microgrid using the proposed RWFNN controller shown in Figs. 5(e) and 5(f) are much improved during the mode switching owing to the robustness and the adaptivity of the proposed RWFNN controller. Thus, the seamless switching of the microgrid can be achieved.

V. CONCLUSIONS

In this study, a grid-connected microgrid with virtual inertia using master/slave control has been successfully developed and implemented via PSIM. In order to improve the reactive power control of the microgrid in grid-connected mode and the transient responses during the mode switching, an online trained RWFNN is proposed and to replace the conventional PI controller in the storage system of the microgrid. The effectiveness and the feasibility of the grid-connected microgrid with virtual inertia using the proposed RWFNN controller are certified by the simulation results. Major contributions of this study are: (i) the successful development of a microgrid with virtual inertia; (ii) the successful development of the proposed online trained RWFNN controller; (iii) the successful implementation of the microgrid using the proposed RWFNN controller for the improvements of reactive power control and voltage control of the microgrid.

REFERENCES

[1] J. Liu, Y. Miura, and T. Ise, "Comparison of dynamic characteristics between virtual synchronous generator and droop control in inverter-based distributed generators," *IEEE Trans. Power Electron.*, vol, 31, no. 5, pp. 3600-3611, May 2015.

[2] G. C. Kryonidis, E. O. Kontis, A. I. Chrysochos, K. O. Oureilidis, C. S. Demoulias, and G. K. Papagiannis, "Power flow of islanded AC microgrids: revisited," *IEEE Trans. Smart Grid*, vol 9, no. 4, pp. 3903-3905, July 2018.

[3] C. S Wang, X. S. Yang, Z. Wu, Y. B. Che, L. Guo, S. H. Zhang, and Y. X. Liu, "A highly integrated and reconfigurable microgrid testbed with hybrid distributed energy sources," *IEEE Trans. Smart Grid*, vol. 7, no. 1, pp. 451-459, January 2016.

[4] K. Yu, Q. Ai, S. Wang, J. Ni, and T. Lv, "Analysis and optimization of droop controller for microgrid system based on small-signal dynamic model," *IEEE Trans. Smart Grid*, vol. 7, no. 2, pp. 695-705, March 2016.

[5] J. Alipoor, Y. Miura, and T. Ise, "Power system stabilization using virtual synchronous generator with alternating moment of inertia," *IEEE J. Emerg. Sel. Top. Power Electron.*, vol. 3, no. 2, pp. 451-458, June 2015.

[6] L. Y. Lu and C. C. Chu, "Consensus-based secondary frequency and voltage droop control of virtual synchronous generators for isolated AC micro-grids," *IEEE J. Emerg. Sel. Top. Circuits Syst.*, vol. 5, no. 3, pp. 443-455, September 2015.

[7] Y. Ma, W. Cao, L. Yang, F. Wang, and L. M. Tolbert, "Virtual synchronous generator control of full converter wind turbines with short-term energy storage," *IEEE Trans. Ind. Electron.*, vol. 64, no. 11, pp. 8821-8831, November 2017.

[8] Q. C. Zhong, G. C. Konstantopoulos, B. Ren, and M. Krstic, "Improved synchronverters with bounded frequency and voltage for smart grid integration," *IEEE Trans. Smart Grid*, vol. 9, no. 2, pp. 786-796, March 2018.

[9] T. Kerdphol, F. S. Rahman, Y. Mitani, M. Watanabe, and S. Küfeoğlu, "Robust virtual inertia control of an islanded microgrid considering high penetration of renewable energy," *IEEE Access*, vol. 6, pp. 625-636, February 2018.

[10] S. Y. Chen, Y. H. Hung, S. S. Gong, "Speed control of vane-type air motor servo system using proportional integral derivative based fuzzy neural network," *Int. J. Fuzzy Syst*, vol. 18, no. 6, pp. 553–564, Jan. 2016.

[11] Y. Li, H. L. Wei, S. A. Billings, "Identification of time-varying systems using multi-wavelet basis functions," *IEEE Trans. Control Syst. Technol.*, vol. 19, no. 3, pp. 656–663, May 2011.

[12] M. Shahriari-kahkeshi, F. Sheikholeslam, "Adaptive fuzzy wavelet network for robust fault detection and diagnosis in non-linear systems," *IET Control Theory Appl.*, vol. 8, no. 15, pp. 1487–1498, Oct. 2014.

[13] S. H. Park, S. I. Han, "Robust-tracking control for robot manipulator with deadzone and friction using backstepping and RFNN controller," *IET Control Theory Appl.*, vol. 5, no. 12, pp. 1397–1417, Aug. 2011.

[14] S. Ganjefar, M. Tofighi, "Single-hidden-layer fuzzy recurrent wavelet neural network: applications to function approximation and system identification," *Inf. Sci.*, vol. 294, pp. 269–285, Feb. 2015.

[15] F. J. Lin, K. C. Lu, and B. H. Yang, "Recurrent fuzzy cerebellar model articulation neural network based power control of single-stage three-phase grid-connected photovoltaic system during grid faults," *IEEE Trans. Ind. Electron.*, vol. 64, no. 2, pp. 1258-1268, February 2017.

[16] S. Teimourzadeh, F. Aminifar, M. Davarpanah, and M. Shahidehpour, "Adaptive control of microgrid security," *IEEE Trans. Smart Grid*, vol. 9, no. 4, pp. 3909-3910, July 2018.

[17] J. Fang, H. Li, Y. Tang, and F. Blaabjerg, "Distributed power system virtual inertia implemented by grid-connected power converters," *IEEE Trans. Power Electronic.*, vol. 33, no. 10, pp. 8488-8499, October 2018.